ACS APPLIED MATERIALS & INTERFACES

Research Article

www.acsami.org

Coat Protein-Dependent Behavior of Poly(ethylene glycol) Tails in Iron Oxide Core Virus-like Nanoparticles

Andrey G. Malyutin,[†] Hu Cheng,[§] Olivia R. Sanchez-Felix,[†] Kenneth Carlson,[†] Barry D. Stein,[∥] Petr V. Konarev,[‡,⊥] Dmitri I. Svergun,[‡] Bogdan Dragnea,*[,†] and Lyudmila M. Bronstein*[,†,#]

[†]Department of Chemistry, Indiana University, 800 East Kirkwood Avenue, Bloomington, Indiana 47405, United States

[‡]EMBL, Hamburg Outstation, Notkestraße 85, D-22603 Hamburg, Germany

[§]Department of Psychological and Brain Sciences, Indiana University, 1101 East Tenth Street, Bloomington, Indiana 47403, United States

[∥]Department of Biology, Indiana University, 1001 East Third Street, Bloomington, Indiana 47405, United States

[#]Department of Physics, Faculty of Science, King Abdulaziz University, Jeddah 21589, Saudi Arabia

Supporting Information

ABSTRACT: Here we explore the formation of virus-like nanoparticles (VNPs) utilizing 22−24 nm iron oxide nanoparticles (NPs) as cores and proteins derived from viral capsids of brome mosaic virus (BMV) or hepatitis B virus (HBV) as shells. To accomplish that, hydrophobic FeO/Fe_3O_4 NPs prepared by thermal decomposition of iron oleate were coated with poly(maleic acid-*alt*-octadecene) modified with poly(ethylene glycol) (PEG) tails of different lengths and grafting densities. MRI studies show high r_2/r_1 relaxivity ratios of these NPs that are practically independent of the polymer coating type. The versatility and flexibility of the viral capsid protein are on display as they readily form shells that exceed their native size. The location of the long PEG tails upon shell formation was investigated by electron microscopy and small-angle X-ray scattering. PEG tails were located differently in the BMV and HBV VNPs, with the BMV VNPs preferentially entrapping the tails in the interior and the HBV VNPs allowing the tails to extend through the capsid, which highlights the differences between intersubunit interactions in these two icosahedral viruses. The robustness of the assembly reaction and the protruding PEG tails, potentially useful in modulating the immune response, make the systems introduced here a promising platform for biomedical applications.

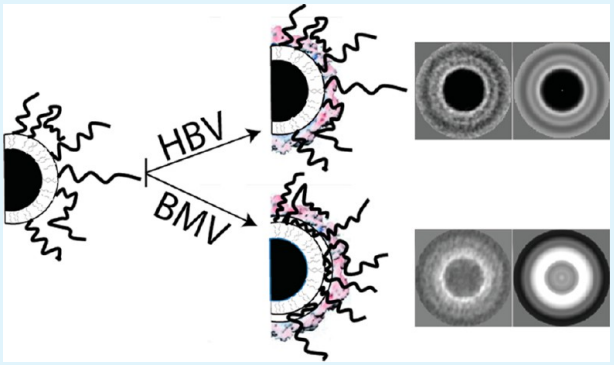

KEYWORDS: *virus-like nanoparticles, magnetic nanoparticles, core−shell, iron oxide, brome mosaic virus, hepatitis B virus, poly(ethylene glycol) (PEG), poly(maleic anhydride-alt-1-octadecene)*

INTRODUCTION

Iron oxide nanoparticles (NPs) are highly versatile materials that benefit from extensive shape and size control, tunable magnetism, and low toxicity leading to a wide variety of potential applications.[1−3] These applications range from magnetic storage materials to catalysts and contrast agents for magnetic resonance imaging.[4−7] The challenge in employing iron oxide NPs is in providing sufficient surface functionalization needed for specific applications. To make the particles biocompatible, a variety of coatings have been examined including dextran, PEGylated phospholipids (PEG is poly(ethylene glycol)), and chitosan to name the few.[8−10] Amphiphilic copolymers forming double hydrophobic bilayers with hydrophobic NPs have also been explored.[10−13]

Functionalization approaches aimed at biological applications further benefit from the coating modification for additional functionality. For instance, folic acid can be attached for added specificity toward cancer cells overexpressing folate receptors; PEG chains provide additional screening from the removal of the particles by the reticuloendothelial system; and fluorescent groups provide a tracking capability.[14−17]

Another method for further functionalization is through encapsulation of biocompatible NPs in protein shells, specifically those derived from viruses.[18,19] Many viruses are inherently monodisperse and biocompatible, displaying tissue targeting specificity. They can be readily produced in large amounts and susceptible to further modifications either through genetic or chemical means.[20−22] Viruses have been extensively studied for use in biomedical applications, such as gene therapies, drug delivery, and magnetic resonance imaging (MRI).[23−25] Much of the previous work has focused on anchoring MR active cations, such as gadolinium, on viral

Received: March 15, 2015
Accepted: May 19, 2015
Published: May 19, 2015

DOI: 10.1021/acsami.5b02278
ACS Appl. Mater. Interfaces 2015, 7, 12089−12098

capsids. A potentially safer and more biocompatible approach lies in encapsulating iron oxide NPs on the interior of viral capsids. For most viruses, however, this can only be achieved at low ionic strengths with hydrophilic particles carrying sufficient surface charge density to neutralize the basic protein residues that would normally associate with nucleic acid.[18,26−28] Specific mechanistic questions concerning systemic, long-range movement of viruses could be directly addressed and benefit from the high magnetic contrast and structural virus mimics afforded by VNPs. Moreover, combining the virus innate tissue tropism with the possibility of magnetic hyperthermia afforded by benign iron oxide NPs could lead to localized, minimally invasive antitumor agents.

Previously, we have explored formation of water-soluble iron oxide NPs utilizing amphiphilic copolymer, poly(maleic anhydride-*alt*-1-octadecene) (PMAOD), and further PMAOD modified with 5,000 Da MW PEG tails.[13,29,30] It is noteworthy that PMAOD is commercially available and inexpensive. Coating of NPs by PMAOD and PMAOD-PEG is the result of hydrophobic interactions between oleic acid on the surface of NPs and the cetyl tails of octadecene in PMAOD. The grafted PEG tails and the hydrolysis of maleic anhydride groups when the polymer is mixed with NPs allowed for electrostatic and steric stabilization of the latter. Moreover, as was demonstrated earlier, NPs functionalized with PMAcOD-PEG (PMAcOD stands for poly(maleic acid-*alt*-1-octadecene)) containing 60% of the 5,000 Da PEG tails maintained stability in a wide range of buffers. In the present work, we coated NPs with modified PMAcOD using both 5,000 and 9,000 Da MW PEG, evaluated the MRI contrast enhancement, and studied encapsulation of biocompatible iron oxide NPs with capsid proteins of brome mosaic virus (BMV)—a plant virus—and hepatitis B (HBV)—a mammalian virus. BMV is representative of a broad class of single-stranded RNA viruses including important mammalian pathogens. HBV is an enveloped small virus, which carries a circular DNA genome. HBV represents a serious human health concern and is one of the best-studied human viruses. Therefore, these viruses were chosen for our study due to the fact that they are model systems, each being representative for a broader class.

Despite their structural and native cargo differences, in both cases, virus coat proteins form shells around the iron oxide cores despite the presence of PEG tails. Indeed, one would expect hindered formation of VNPs due to the size of the tail and the fact that the negative charges, necessary for the coat formation, are located at the base of the tails instead of periphery. We demonstrate here, for the first time, different packing behavior of PEG tails upon shell formation depending on the virus type. Considering that PEG tails may increase versatility and stability of virus capsids[31] and the magnetic cores demonstrate exceptional MRI responses, the VNPs fabricated are an excellent platform for biomedical applications.

MATERIALS AND METHODS

Materials. $FeCl_3{\cdot}6H_2O$ (98%), oleic acid (90%), docosane (99%), Trizma base (99.9%), cesium chloride (98%), magnesium acetate tetrahydrate (99%), Tris-borate-EDTA 10×, poly(maleic anhydride-*alt*-1 octadecene) of 30,000−50,000 Da MW, and methoxypoly(ethylene glycol) amine of 5,000 Da MW were purchased from Sigma-Aldrich and used as received. Sodium oleate (>97%, TCI America) was also used without purification. Methoxypoly(ethylene glycol) amine of 9,000 Da MW was purchased from Polymer Source Inc. and used as received. Potassium chloride (99%), sodium citrate dehydrate (99%), and sodium chloride (99%) were purchased from Mallinckrodt Chemicals and used as received. Magnesium chloride 6-hydrate (99%) was purchased from J.T. Baker and used as received. Hexanes (85%), ethanol (95%), acetone (99.8%), sodium acetate anhydrous (99%), and sodium phosphate monobasic monohydrate (98%) were from EMD and used as received. Chloroform (Mallinckrodt, 100%), oleic acid (TCI, 95%), and oleic acid sodium salt (ScienceLab.com, 95%) were used without purification.

Synthesis of Iron Oxide Nanoparticles. NPs of ∼24 nm in diameter were prepared via thermal decomposition of iron oleate in docosane in the presence of oleic acid as described elsewhere.[32] Briefly, in a typical experiment, 1.93 g of iron oleate complex, 1.96 mL (6.2 mmol) of oleic acid, and 7.54 g (24.3 mmol) of docosane were placed in a three-neck round-bottom flask (with elongated necks) equipped with a magnetic stir bar, a reflux condenser connected to a vacuum line, and two septa, one of which contains an inserted temperature probe protected with a glass shield. The reaction flask was evacuated and filled with argon three times. Then the reaction solution was heated to 60 °C to melt docosane and allow dissolution of the components under stirring. After that the temperature was increased to about 370 °C with a heating rate of 3.3 °C/min under stirring (using temperature controller and set temperature of 380 °C) and kept refluxing for 3 min. After cooling to 50 °C, the reaction solution was transferred to a vial and stored at 4 °C.

Virus Preparation. The *Agrobacterium*-transfection method[33] was used for expression of BMV in *Nicotiana benthamiana*. Plants were allowed to grow for 7 days postinfection. The leaves were then collected and homogenized in virus buffer (0.25 M NaOAc, 0.01 M $MgCl_2$, pH 4.5). The solution was centrifuged on a Beckman TA-10.250 rotor at 5,000 rpm for 25 min. The supernatant was then centrifuged on a Beckman SW32 rotor for 3 h at 26,000 rpm on a 10% sucrose cushion. The pellet was resuspended in 38.5% CsCl, and the virus band was isolated by centrifugation for 24 h on a Beckman TI-71 rotor at 45,000 rpm. The band was dialyzed against SAMA buffer (0.05 M NaOAc, 0.008 M $Mg(OAc)_2$, pH 4.5), with three changes. The virus was further purified by FPLC (AktaPurifier) equipped with a Superose-6 column. Virus was disassembled and RNA precipitated by dialysis against disassembly buffer (0.5 M $CaCl_2$, pH 7.4), with three changes of the buffer. RNA was removed by centrifugation on a Beckman TLA 110 rotor at 35,000 rpm for 30 min. The supernatant containing protein dimers was dialyzed against Tris (0.01 M Tris, pH 7.4) buffer and then TNKM (0.05 M Tris, 0.05 M NaCl, 0.01 M KCl, 0.005 M $MgCl_2$, pH 7.4) for 24 h each.

Details for expression of Hepatitis B coat protein are provided elsewhere.[34] A full capsid protein sequence with C-terminal domain codon optimized for expression in *Escherichia coli* (*E. coli*) was used. Cells were lysed by sonication, and HBV capsids were isolated by centrifugation. Capsids were further purified by size exclusion chromatography and stored at −80 °C until needed.

Preparation of PMAOD-PEG Copolymers. Notations of "P" and "N" are reserved for PMAOD-PEG5000 (P#) and PMAOD-PEG9000 (N#), respectively. Solutions were prepared at molar ratios of 1:30 (N2), 1:60 (P3,N3), and 1:80 (P4) PMAOD to PEG. Initially PMAOD stock solution of 10 mg/mL (2.5×10^{-4} mmol/mL) was prepared in chloroform and stirred overnight. The PMAOD-PEG stock solutions were prepared in 2 mL aliquots with PMAOD concentration of 2.5 mg/mL. In a typical preparation of a P3 solution, 37.5 mg (7.5×10^{-3} mmol) of PEG5000 was dissolved in 1.5 mL of $CHCl_3$. The 0.5 mL of the 10 mg/mL PMAOD solution (1.25×10^{-4} mmol in PMAOD:P3) was then added and the solution was stirred overnight.

Encapsulation of Iron Oxide NPs with PMAOD-EG. For NP encapsulation 1:0.5 mass ratio of NPs to PMAOD-PEG was maintained. In a typical preparation, 0.3 mL of purified NPs (0.5 mg) in chloroform was combined with 0.1 mL of the PMAOD-PEG stock solution (0.25 mg of the polymer) and stirred for 30 min. DMSO (2 mL) was added, and the solution was stirred for another 30 min. The solution was then split into several wide vials to increase the surface area, and chloroform was evaporated under vacuum for 3−4 h. The remaining solution was combined in a single vial, and 10 mL of 20% TBE buffer was rapidly added. The solution was stirred overnight.

DOI: 10.1021/acsami.5b02278
ACS Appl. Mater. Interfaces 2015, 7, 12089−12098

The following day, the solution was dialyzed against deionized water for 24 h to remove DMSO, and then the polymer excess was removed by two cycles of ultracentrifugation at 10,000 rpm for 15 min. Aggregates, if any, were removed by a 10 min 3,000 rpm centrifugation cycle.

BMV VNP Assembly. NPs and BMV dimers were mixed at a ratio of 1 to 360 in TNKM buffer (0.05 M Tris-HCl, 0.05 M NaCl, 0.01 M KCl, 0.005 M $MgCl_2$) to make a solution volume of 100 μL at the protein concentration of 0.5 mg/mL. The solution was dialyzed in TNKM for 24 h. The mixture was then dialyzed again at pH 4.6 and low ionic strength SAMA buffer (0.05 M NaOAc, 0.008 M $Mg(OAc)_2$). In a typical assembly, 0.125 mg of NPs were used ($\sim 3.2 \times 10^{13}$ NP/mL).

HBV VNP Assembly. Viral capsids, composed of full length protein subunits and random *E. coli* RNA, were dialyzed against 1.5 M guanidine HCl buffer (0.5 M LiCl, 50 mM HEPES, 2 mM DTT, pH 7.5) to disassemble the capsids into dimers and precipitate the RNA. The RNA was then removed by centrifugation, and the protein dimers were further purified by HPLC. The dimers were then mixed with the iron oxide NPs at the same ratio as that used with BMV proteins and dialyzed against low ionic strength buffer (0.1 M NaCl, 50 mM Tris, pH 7.5).

CHARACTERIZATION

ζ-Potential and DLS Measurements. ζ-potential and DLS measurements were performed on a Malvern Zetasizer Nano ZS instrument. For DLS measurements, the sample was diluted in 18.2 MΩ water and the data from at least three measurements were averaged. Intensity and volume distributions of the particle sizes were recorded. The ζ-potential was measured at pH 7.4. The data were processed using the absorption coefficient of bulk iron oxide, the indices of refraction of iron oxide and solvent, and the viscosity of the pure water. The Smoluchowski approximation was used to convert electrophoretic mobility to a ζ-potential.

Electron Microscopy. Grids for electron microscopy were prepared by applying 4 μL of sample to a freshly glow discharged, in-house-prepared continuous carbon film on a 200 mesh copper grid. For nanoparticle samples in chloroform, no blotting or staining was necessary. Aqueous samples were blotted after 30 s, followed by 10 s staining with a 4 μL drop of 3% uranyl acetate. Images were acquired on a JEOL JEM1010 instrument at accelerating voltage of 80 kV. Images were analyzed using ImageJ software (NIH) to estimate NP diameters. Between 150 and 300 NPs were used for this analysis.

For rotational averaging, individual particles were boxed out, averaged, and rotationally averaged using the EMAN software package.[35] Line profiles were produced using IgorPro (Wavemetrics) software.

Thermal Gravimetric Analysis. TGA was performed on TGAQ5000 IR (TA Instruments, Inc.). TGA samples were prepared by evaporation of NPs solutions in 100 μL platinum pans, by filling the pan and allowing chloroform to evaporate. The experiments were carried upon heating to 700 °C at a rate of 10.0 °C/min.

Small-Angle X-ray Scattering. Synchrotron SAXS measurements were performed at the European Molecular Biology Laboratory (EMBL) on the storage ring DORIS III of the Deutsches Elektronen Synchrotron (DESY, Hamburg, Germany) on the X33 beamline[36] equipped with a robotic sample changer and a 1 M PILATUS detector (DECTRIS, Baden, Switzerland). Samples were measured at 10 °C in a concentration range of 0.5−2.0 mg/mL. Scattering was recorded in the range of the momentum transfer $0.1 < s < 6.0$ nm^{-1}, where $s = (4\pi \sin\theta)/\lambda$, 2θ is the scattering angle, and $\lambda = 0.15$ nm is the X-ray wavelength. The measurements were carried out in a vacuum capillary; no measurable radiation damage was detected by comparison of 10 successive time frames with 15 s exposures. The experimental scattering profiles from all solutes were corrected for the background scattering from the appropriate solvent and processed using standard procedures.[37] The concentration dependence was absent for all solutes, and the highest concentration data were used for further analysis. The radius of gyration, R_g, and the maximum particle dimension, D_{max}, were evaluated using GNOM software.[38] All SAXS patterns were analyzed using the program MIXTURE from the software suite PRIMUS.[37] A polydisperse spherical particle system was used to fit the data, whereby size polydispersity was parametrized with a monomodal Gaussian distribution. To take into account the formation of clusters, the spheres were allowed to constitute dumbbells and tetrahedrons, and the average distance between the particles and its variation were also refined by MIXTURE while fitting the experimental data.

Magnetic Resonance Imaging. T_1 and T_2 relaxation times were measured with a 3T TIM Trio magnetic resonance imaging (MRI) scanner (Siemens Medical Solutions, Erlangen, Germany). For T_1 relaxation time measurements, a series of T_1-weighted images were obtained using turbo spin echo sequence with inversion recovery and the following parameters: TR/TE = 15000/(10 ms), T_I = 100, 200, 400, 800, 1600, 3200, 4000, 5000, 6000, and 10000 ms, flip angle = 180°, turbo factor = 7, slice thickness = 2 mm, and in-plane resolution = 0.935 mm × 0.935 mm. The voxel-wised image intensities, S, with respect to different T_I were fit to eq 1 using least-squares curve fitting to obtain the T_1 value.

$$S = M_0|1 - 2e^{-TI/T_1} + e^{-TR/T_1}| \quad (1)$$

For T_2 relaxation time measurements, a series of T_2-weighted images were obtained with spin echo sequence and parameters: TR = 4000 ms, TE = 11, 22, 44, 88, 160, and 240 ms, flip angle = 90°, slice thickness = 3 mm, and in-plane resolution = 1.875 mm × 1.875 mm. S with respect to different TE were fit to eq 2 using least-squares curve fitting to obtain the T_2 value.

$$S = M_0 e^{-TE/T_2} \quad (2)$$

RESULTS AND DISCUSSION

NP Functionalization by Modified PMAOD. To impart water solubility and biocompatibility, iron oxide NPs of 22−24 nm in size, prepared via thermal decomposition of iron oleate were coated with a double hydrophobic layer using amphiphilic copolymers as discussed elsewhere.[29] As previously determined by X-ray powder diffraction, the NPs consist of FeO and likely Fe_3O_4 with the former phase prevailing.[10] As-synthesized NPs are coated with oleic acid and only soluble in organic solvents.

The maleic anhydride moiety of PMAOD (Figure 1A) is readily susceptible to a reaction with an amino group, resulting in the formation of carboxyl and amide groups (Figure 1B).[29] After grafting, the remaining anhydride moieties are hydrolyzed in the TBE buffer in the presence of NPs, resulting in the formation of amphiphilic PMAcOD-PEG coated iron oxide NPs. Earlier we reported a modification of PMAOD with 5,000 Da PEG with grafting density varied between 20 and 80%.[29] It is noteworthy that only NPs modified with 60 and 80% of the 5,000 Da PEG tails were stable in buffers. On the other hand, in

DOI: 10.1021/acsami.5b02278
ACS Appl. Mater. Interfaces 2015, 7, 12089−12098

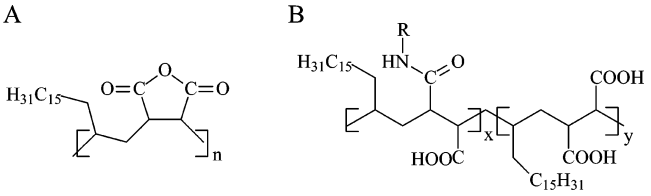

Figure 1. Repeating units of PMAOD (A) and PMAcOD-PEG (B). In B "x" is the degree of the PEG grafting, while $y = n - x$. R is PEG (5,000 or 9,000 Da).

the case of the 9,000 Da PEG tails, even 30% of PEG tails allowed stability in a wide range of buffers. This behavior determined the choice of functionalized NPs (Table 1) for virus

Table 1. Amounts of Copolymer Molecules per NP and the Weight Losses for NPs Coated with PMAcOD-PEG

sample[a]	weight loss from TGA (%)	macromolecules per NP	MW of macromolecules (kDa)	total polymer weight per NP (mg)
NP-P3	32.3	21	380	1.33×10^{-14}
NP-P4	34.3	19	490	1.54×10^{-14}
NP-N2	30.4	15	363	9.05×10^{-15}
NP-N3	21.5	3	686	3.66×10^{-15}

[a]NP-P3 stands for the NPs functionalized with PMOAcD containing 60% of the 5000 Da PEG tails; NP-P4 is for the NPs functionalized with PMOAcD containing 80% of the 5000 Da PEG tails; NP-N2 is for the NPs functionalized with PMOAcD containing 30% of the 9000 Da PEG tails; NP-N3 stands for the NPs functionalized with PMOAcD containing 60% of the 9000 Da PEG tails.

assembly studies. NP-N2 and NP-N3 (30 and 60% of 9,000 Da PEG tails) as well as NP-P3 and NP-P4 (60 and 80% of 5,000 Da PEG tails) (see Table 1 footnote *a*) represent minimum and maximum amounts of PEG tails allowing formation of NPs which are stable in buffers and are sufficiently negatively charged to be coated with viruses. NP-P3 and NP-N3 with the same grafting density allowed a comparison of the data on BMV and HBV VNPs.

Figure S1 (the Supporting Information, SI) shows a representative TEM image of the N2 functionalized NPs (NP-N2). The NPs remain primarily dispersed even on the TEM grid. Dynamic light scattering and ζ-potential measurements (Table S1 and the text, SI) were used to characterize the coating of the 24 nm iron oxide NPs with PMAcOD-PEG at variations of PEG length and a degree of grafting. All coated NPs are negatively charged (Table S1, SI). The small differences in hydrodynamic diameters of the coated NPs could be explained by different folding of the PEG tails. TGA was used to quantitatively assess the number of PMAOD-PEG chains on the surface of the iron oxide cores. The number of the oleic acid molecules was found to be 7.34 molecules/nm^2 regardless of the particle type.[29] The weight loss from TGA and the calculated amounts of copolymer molecules are shown in Table 1.

As the number and molecular weight of PEG molecules increase, the number of macromolecules per particle decreases. There are about 20 copolymer molecules for the P coated samples. This value decreases for the N2 coated NPs to 15 and to 3 for the N3 coated particles. A similar trend was observed earlier for NPs coated with PMAcOD-PEG with the 5,000 Da MW PEG tails.[29] The trend can be explained through a more hydrophilic NP environment associated with additional and/or longer PEG tails which prevent further adsorption of the amphiphilic copolymers on the NP surface.

MRI Characterization of Functionalized NPs. To evaluate MRI contrast properties of iron oxide NPs coated with PMAcOD-PEG, MR relaxivities and map images of the coated NPs were investigated. Experiments were performed in a clinical 3T MR scanner at room temperature. The dose-dependent contrast change can be seen qualitatively in Figure 2.

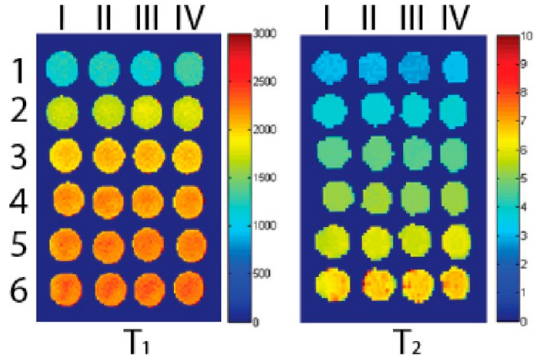

Figure 2. Longitudinal T_1 map and transverse T_2 map of NP-P3 (I), NP-P4 (II), NP-N2 (III), and NP-N3 (IV) NPs. Scale bar in the T_1 map is linear, while in the T_2 map it is logarithmic. Sample concentrations: (1) 0.93, (2) 0.37, (3) 0.14, (4) 0.06, (5) 0.04, and (6) 0.01 mM Fe.

To quantitatively compare the samples, inverse relaxation times $(1/T_{n(\text{samples})} - 1/T_{n(\text{solvent})}$, where n is 1 or 2) were plotted as a function of the iron concentration (Figure 3). The slopes of the fits were used to calculate the longitudinal r_1 and transverse r_2 relaxivities, and the r_2/r_1 ratio can be used to compare the effectiveness of T_2 contrast agents. The r_2/r_1 ratio is very similar for all four samples (Table 2), indicating that the

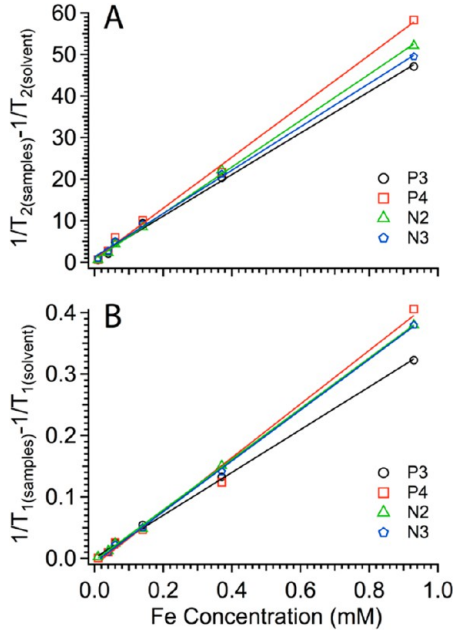

Figure 3. Plots of inverse relaxation times (A) $(1/T_{1(\text{samples})} - 1/T_{1(\text{solvent})})$ and (B) $(1/T_{2(\text{samples})} - 1/T_{2(\text{solvent})})$ as a function of iron concentration. The slopes correspond to (A) the longitudinal r_1 and (B) the transverse r_2 relaxivities, respectively.

DOI: 10.1021/acsami.5b02278
ACS Appl. Mater. Interfaces 2015, 7, 12089−12098

Table 2. MRI Characteristics of PMAcOD-PEG Coated NPs Reported in This Work and Elsewhere

sample	grafting (%)	r_1 (mM^{-1} s^{-1})	r_2 (mM^{-1} s^{-1})	r_2/r_1
NP-P3	60	0.348	49.88	143.3
NP-P4	80	0.436	61.38	140.8
NP-N2	30	0.412	55.81	135.5
NP-N3	60	0.413	52.18	126.3
Ferumoxtran-10[41]		9.9	65	6.8
Supravist,[42]		38	10.7	3.55
Fe_3O_4 dye[43]		16	45	2.8
Fe_3O_4@Au@Glu[44]		10	160	16.0
Au@$MnFe_2O_4$[45]		6.01	83.3	13.9

effect of PEG chains of different lengths on the magnetic properties of the cores is small. The observed differences in the magnitude of r_2 likely reflect a change of diffusion coefficient (D) in eq 3:

$$r_2 = \frac{1}{T_2} = \frac{a}{d_{NP}D}\gamma^2\mu^2 C_{NP} J(\omega, \tau_D) \quad (3)$$

where a is the constant, d_{NP} is the NP diameter, μ is the NP magnetic moment, γ is the gyromagnetic ratio of the water proton, C_{NP} is the NP concentration, and $J(\omega,\tau_D)$ is the spectral density function.[39] Assuming the changes in the diffusion coefficient are purely dependent on volume, for cores of the same size, and assuming a similar coat density, the order is NP-P4 > NP-P3 > NP-N2 > NP-N3 (Table 1). This is what we observe in the r_2 relaxivities, with the exception of NP-P3.

To the best of our knowledge, these r_2/r_1 values are greater than any values reported in literature for hydrophilic particles that are available commercially, in clinical investigations, or in laboratory studies (Table 2).[40−43]

VNP Formation with PMAcOD-PEG Coated NPs. Figures 4 and 5 clearly demonstrate formation of VNPs for both viruses. Indeed, in addition to the white shells around NPs seen in Figure S1 (SI), an additional shell is developed upon VNP formation. The thickness of this added second shell (~5 nm) is consistent with it being made of capsid proteins.[46,47] It is noteworthy that the variable NP core contrast is due to the interference and different orientation of NPs. Remarkably, despite the presence of a considerable number of long PEG tails, P3, P4, N2, and N3 functionalized NPs promote formation of BMV and HBV coat protein shells.

In our preceding works we have reported on VNP formation with the sizes that greatly exceed the native size of the virions using PEGylated phospholipids (PEG 2000 Da MW) with terminal carboxyl groups.[26,28] Please note, however, that for the P3, P4, N2, and N3 functionalized NPs, the NP shell contains longer PEG tails and the negative charges, which are considered

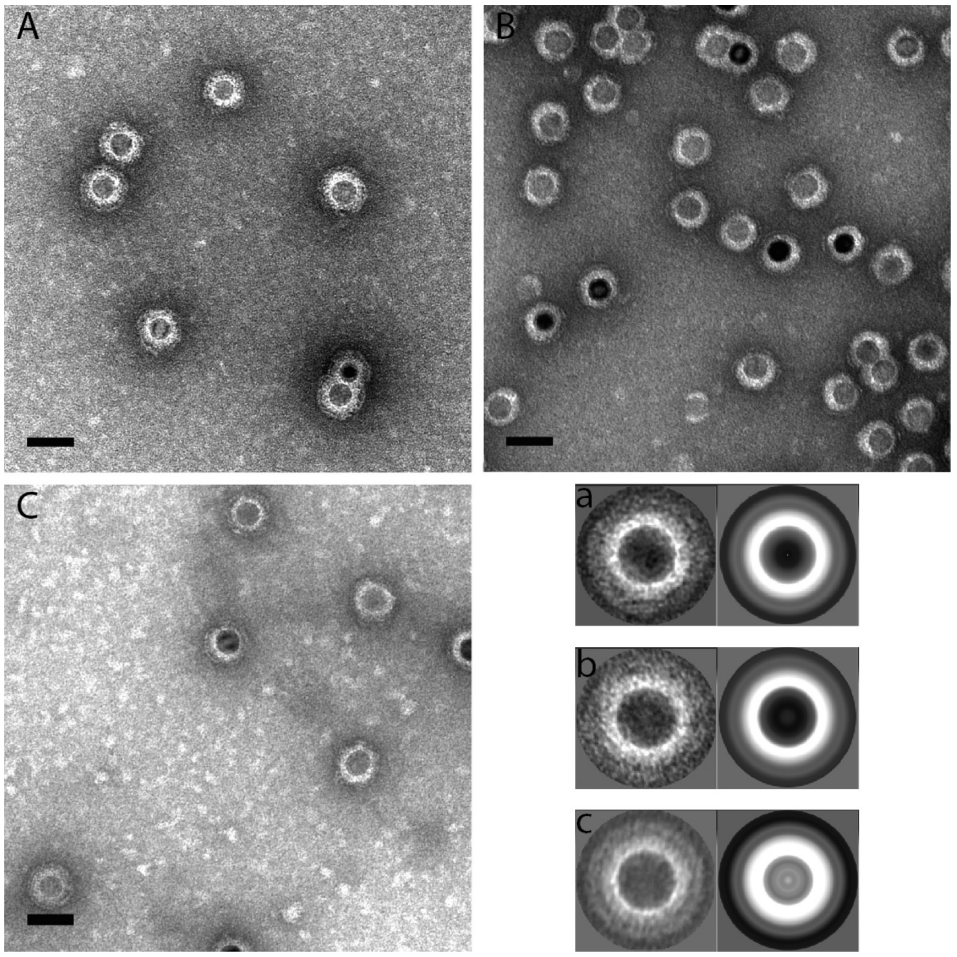

Figure 4. BMV encapsulated P3 (A), P4 (B), and N2 NPs (C). The sizes of the VNPs formed are 42.8 ± 4.9, 46.1 ± 6.1, and 48.1 ± 4.6 nm, respectively. Class averages and rotational averages for each set are shown in panels a−c. Scale bars are 50 nm. The variable NP core contrast is due to the interference and different orientation of NPs.

DOI: 10.1021/acsami.5b02278
ACS Appl. Mater. Interfaces 2015, 7, 12089−12098

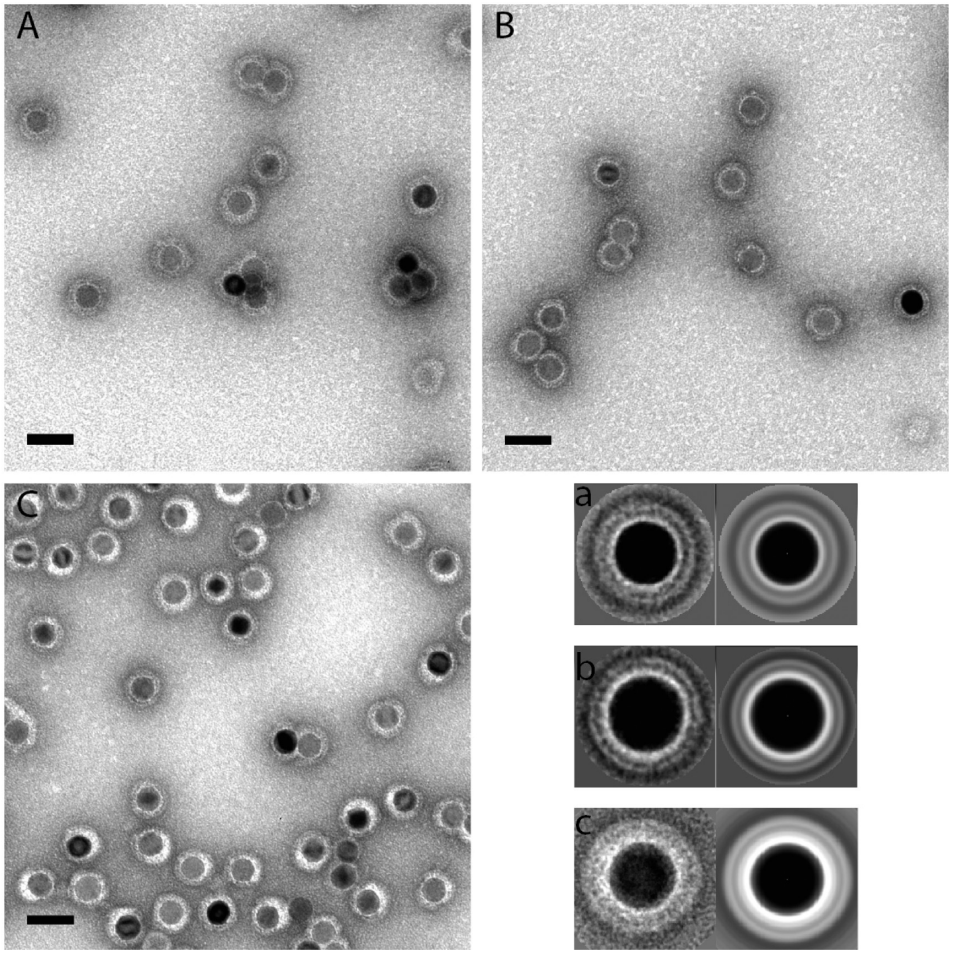

Figure 5. HBV encapsulated P4 (A), N2 (B), and N3 NPs (C). The sizes of the VNPs formed are 39.9 ± 5.0, 41.0 ± 5.4, and 43.3 ± 5.5 nm, respectively. Class averages and rotational averages for each set are shown in panels a–c. Scale bars are 50 nm.

to be crucial for the virus self-assembly due to electrostatic interactions, are located on the iron oxide NP surface, not at the PEG exterior. Hence, the question arises: where are the PEG tails located? A TEM analysis approach was used to attempt to answer this question.

It is worth noting that the outer and inner diameters of native $T = 3$ BMV and $T = 4$ HBV are ~28/18[46] and ~35/26 nm,[47] respectively. VNP diameters of BMV coated NPs range from 42.8 to 48.1 nm (depending on the polymer type). For HBV coated NPs, diameters range from 39.9 to 43.1 nm (Table 3).

Table 3. VNP Size Distribution

	BMV		HBV	
sample	diam (nm)	std dev (%)	diam (nm)	std dev (%)
VNP-P3	42.8	4.9	39.9	5.0
VNP-P4	46.1	6.1	42.0	6.2
VNP-N2	48.1	4.6	41.0	5.4
VNP-N3	46.1	9.1	43.3	5.5

The larger sizes of VNPs compared to the wild-type viruses are not surprising considering the iron oxide core size is 22–24 nm. This is consistent with our earlier results for VNPs based on 20 nm iron oxide NPs functionalized with PEGylated phospholipids.[26] It is noteworthy however that the HBV VNPs are systematically smaller than the BMV VNPs (Table 3).

A closer look at the TEM images indicates that BMV and HBV proteins behave differently when they self-assemble around PMAcOD-PEG coated NPs. The distance between the core and protein layer appears to be much greater in BMV, compared to that of the HBV coated NPs, where the protein is much closer to the cores (see Figures 4 and 5a–c and Table 4).

Table 4. BMV and HBV VNP Shell Thickness

	shell total (nm)	
sample	BMV	HBV
VNP-P3	10.9	
VNP-P4	9.7	6.8
VNP-N2	9.3	6.2
VNP-N3		7.7

This suggests a different packing behavior for the PEG tails. The two possibilities are (i) the majority of the PEG tails extend through holes in a protein layer or (ii) preferential or complete packing of the tails between the core and protein, with minimal extension through the protein, takes place (Scheme 1).

BMV and HBV have different folds of their coat proteins. The BMV capsid forms tighter capsomer junctions and contains fewer and smaller pores compared to those of HBV.[46,47] Additionally, BMV self-assembles into capsids of a single size (28 nm), whereas HBV can exist either as ~31 or

DOI: 10.1021/acsami.5b02278
ACS Appl. Mater. Interfaces 2015, 7, 12089–12098

Scheme 1. Two Potential Arrangements of the PEG Tails during VNP Formation[a]

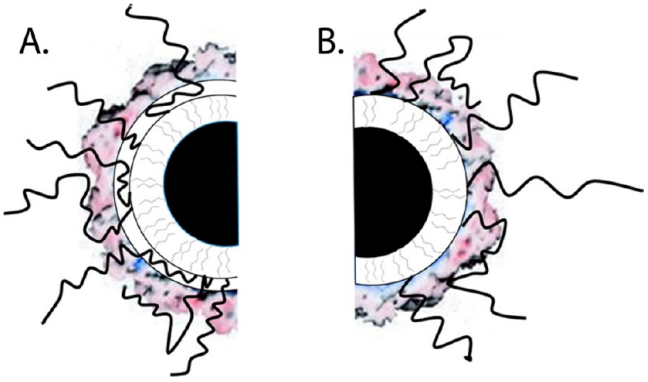

[a](A) PEG tails are completely or partially entrapped between the core and the protein layer. (B) PEG tails primarily penetrate the protein layer.

~35 nm capsids. Therefore, it is probable that BMV is less likely to allow PEG tails to pass through the capsid, which favors trapping the tails. HBV, on the other hand, is more likely to have PEG tails extending through the larger pores at the 5- and pseudo-6-fold vertices, resulting in a smaller separation between the core and the protein. To test this hypothesis, we measured the core–protein separation and the protein shell thickness for the P3, P4, and N2 BMV VNPs and the P4, N2, and N3 HBV VNPs.

This was achieved by measuring the separation between peaks in gray intensities in line profiles through individual VNPs. Figure 6 shows traces for P3, P4, N2, and N3 BMV and

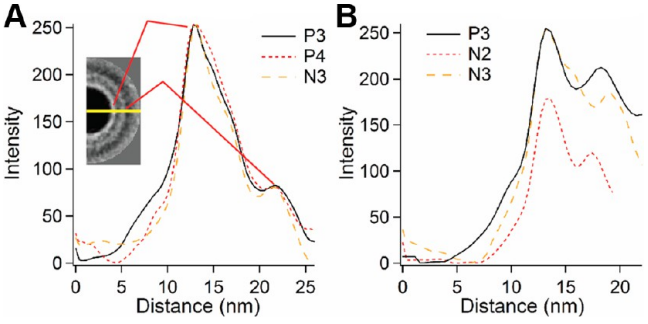

Figure 6. Line profiles of (A) P3, P4, and N3 BMV VNPs and (B) P3, N2, and N3 HBV VNPs. Red lines indicate peaks corresponding to the inner oleic acid–PMAcOD and the protein layers.

HBV VNPs. We assume that the first peak corresponds to the edge of the NP core and the beginning of the oleic acid–PMAcOD-PEG layer, while the second peak corresponds to the protein layer. The total shell thicknesses, from the edge of the core to the outer edge of the protein layer, are summarized in Table 4. It is immediately apparent that this shell is thinner for HBV VNPs than that for BMV VNPs. Further, the thickness of the hydrophobic bilayer formed by oleic acid and cetyl tails of the octadecene units should not exceed ~3.2 nm. This matches two extended C_{18} and C_{16} hydrophobic tails but can be much lower than that due to interdigitation of the tails. As was already mentioned, the protein thickness for BMV and HBV is ~5 nm. Thus, taking into account these sizes, the HBV protein shell preferentially allows for the PEG tail penetration, while the BMV protein shell preferentially traps the tails. Positioning of the PEG tails is important because it may carry an important role in reducing the immunogenicity of virus-based nanoparticles.[48,49]

Characterization of BMV VNPs: SAXS. In order to further understand the effect of protein coating on structural organization, we utilized small-angle X-ray scattering for the BMV VNPs as an example. The scattering patterns of NP-N2, NP-N3, and NP-P3 and VNP-N2, VNP-N3, and VNP-P3 (all VNPs are based on BMV) are presented in Figure 7 (dots with

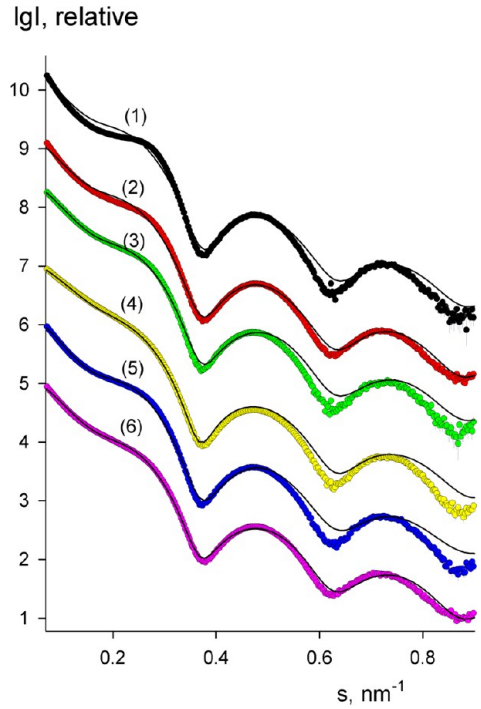

Figure 7. SAXS scattering patterns (dots with experimental error bars) for NP-N2 (curve 1), VNP-N2 (curve 2), NP-N3 (curve 3), VPN-N3 (curve 4), NP-P3 (curve 5), and VNP-P3 (curve 6). The fits (solid curves) were obtained by the modified version of the program MIXTURE[35] using the models of the polydisperse dumbbells and tetrahedrons. The plot displays the logarithm of the scattering intensity as a function of momentum transfer $s = 4\pi \sin(\theta)/\lambda$, where θ is the scattering angle and λ = 0.15 nm is the X-ray wavelength. Successive curves are displaced by one logarithmic order for better visualization.

experimental error bars). All curves display oscillations with alternating and rather symmetric minima/maxima that are typical for spherical particles. At the same time, the very low angle part of the scattering patterns (corresponding to a momentum transfer $s < 0.3$ nm^{-1}) reveals an upward trend, which points to the presence of clusters, similar to those reported elsewhere.[10] The average parameters of individual particles can be estimated by GNOM[38] from the outer parts of the scattering data (beyond $s = 0.3$ nm^{-1}, free from the influence of the interparticle interference in the clusters). The radii of gyration, R_g, of about 9.5 ± 0.3 nm and the maximum sizes D_{max} of about 25 ± 2 nm were found for all constructs. These sizes correlate well with those of the NPs from the TEM measurements, which is not surprising because SAXS "sees" essentially only the scattering from the iron oxide part, which has significantly higher electron density and thus much larger contrast for X-rays than the polymer and protein shells.

DOI: 10.1021/acsami.5b02278
ACS Appl. Mater. Interfaces 2015, 7, 12089–12098

However, although SAXS cannot provide direct data about the organization of the VNPs, useful information can be obtained from cluster analysis, focusing on the shoulder observed in the scattering spectrum at $s \approx 0.26$ nm^{-1}, which corresponds to a distance of $2\pi/0.26 \approx 24$ nm. This distance is close to the average distance between interacting BMV VNPs as seen on the TEM pictures (Figure S1, SI).

Qualitatively, for NPs encapsulated in BMV coat proteins, the shoulder smears out; i.e., the distances between NPs become more variable. In order to obtain quantitative characteristics, the experimental data were fitted with a model accounting for the presence of VNP clusters or "associates". Interestingly, a model containing mixtures of monomeric VNPs and dumbbells (dimeric associates) failed to fit the small-angle portions of the data indicating that higher associates are present. The scattering patterns in Figure 7 can be well-fitted by mixtures of monomers and tetrahedron-like (4-fold) associates yielding the volume fractions of the corresponding components, the average distances between the individual particles inside the associates and its variation (Table 5). The

Table 5. Structural Parameters of the Particles Obtained from Polydisperse Mixtures of Monomeric and Tetrahedron-like Clusters[a]

sample	monomer fraction (%)	tetrahedron fraction (%)	distance (nm)	Δdistance (nm)	χ
NP-N2	57 ± 5	43 ± 5	28.4 ± 0.5	0.4 ± 0.1	3.6
VNP-N2	80 ± 5	20 ± 5	28.3 ± 0.5	0.4 ± 0.1	2.5
NP-N3	49 ± 5	51 ± 5	26.9 ± 0.5	0.8 ± 0.2	1.7
VNP-N3	81 ± 5	19 ± 5	26.8 ± 0.5	1.2 ± 0.2	1.5
NP-P3	34 ± 5	66 ± 5	27.4 ± 0.5	0.9 ± 0.2	1.7
VNP-P3	55 ± 5	45 ± 5	27.2 ± 0.5	1.1 ± 0.2	1.4

[a]Distance, the average distance between the centers of the particles in the tetrahedron clusters; Δdistance, polydispersity degree of the distance.

functionalized NPs tend to form significant fractions (around 50% volume fraction) of the associates, but the BMV VNPs stay largely (to 80% volume fraction) monomeric. The explanation for the observed effect can be 2-fold: (i) BMV shells decrease (screen) the attractive magnetic interactions between the iron oxide NPs and/or (ii) they minimize the interpenetration of the PEG tails leading to association of NPs, although they do not completely suppress it. It is worth noting that the wild-type BMVs do not associate. The obtained average distance (~28 nm) between the individual NPs inside the clusters exceeds the NP sizes due to the presence of the PEG tails. The coating by BMV increases the interparticle distance polydispersity, but still, the NP−NP distances stay smaller than the diameter of the VNPs, suggesting that the NPs are asymmetrically positioned inside the VNPs when they form clusters (e.g., like the dimer in Figure 4A, bottom). The model of interacting clusters allows one to neatly fit all data sets (the deviations of the fit to the experimental data for NP-N2 point to the presence of aggregates still larger than tetramers) and shows good agreement with the TEM data. We believe the formation of mainly single particles for BMV VNPs vs larger and irregular in composition clusters for PMAcOD-PEG coated NPs are important for development of bioprobes with predictable and well-defined properties and behavior. On the other hand, the presence of tetrameric associates can be responsible for higher MRI responses; thus, these associates can have a positive influence on magnetic properties.

CONCLUSIONS

We demonstrated that PMAcOD, modified with 5,000 Da MW and 9,000 Da MW PEG tails, is a multipurpose and inexpensive ligand for biofunctionalization of hydrophobic iron oxide NPs and for further formation of VNPs. An encouraging T_2 MRI response was measured, probably due to large FeO/Fe_3O_4 cores and nonintrusive functionalization. PMAcOD-PEG coated iron oxide NPs were found to be open to further stabilization and functionalization through encapsulation by capsid protein of plant and mammalian viruses—BMV and HBV, respectively. The virus protein coats formed were observed to exceed the virus native size and to accommodate for the long PEG tails in different ways. The PEG tails likely penetrate the protein capsid of HBV. By contrast, in BMV VNPs, the majority of the PEG tails were trapped, presumably between the core and the protein shell. High relaxivity ratios and facile formation of VNPs for both BMV and HBV proteins are highlighting a potential promise for the future development of efficient and harmless MRI contrast agents.

ASSOCIATED CONTENT

Supporting Information

TEM image and the description of the DLS and ζ-potential data. The Supporting Information is available free of charge on the ACS Publications website at DOI: 10.1021/acsami.5b02278.

AUTHOR INFORMATION

Corresponding Authors

*(L.M.B.) E-mail: lybronst@indiana.edu.
*(B.D.) E-mail: dragnea@indiana.edu.

Present Address

⊥Institute of Crystallography RAS, Leninsky pr. 59, 119333 Moscow, Russia.

Funding

This work has been supported, primarily by the U.S. Department of Energy, Office of Science, Basic Energy Sciences, under Aaward DE-SC0010507 (synthesis and electron microscopy studies) and by the Human Frontier Science Program, Research Grant RGP0017/2012 (SAXS).

Notes

The authors declare no competing financial interest.

ACKNOWLEDGMENTS

We thank the IU Nanoscale Characterization Facility and the IU imaging facility at the Department of Psychological and Brain Sciences for access to the instrumentation. We also thank the laboratory of Dr. Adam Zlotnick for providing us with HBV coat protein.

REFERENCES

(1) Schmid, G. *Nanoparticles: From Theory to Application*; Wiley: Hoboken, NJ, USA, 2004.

(2) Briley-Saebo, K.; Bjornerud, A.; Grant, D.; Ahlstrom, H.; Berg, T.; Kindberg, G. M. Hepatic Cellular Distribution and Degradation of Iron Oxide Nanoparticles Following Single Intravenous Injection in Rats: Implications for Magnetic Resonance Imaging. *Cell Tissue Res.* **2004**, *316*, 315−323.

DOI: 10.1021/acsami.5b02278
ACS Appl. Mater. Interfaces 2015, 7, 12089−12098

(3) de Montferrand, C.; Hu, L.; Milosevic, I.; Russier, V.; Bonnin, D.; Motte, L.; Brioude, A.; Lalatonne, Y. Iron Oxide Nanoparticles with Sizes, Shapes and Compositions Resulting in Different Magnetization Signatures as Potential Labels for Multiparametric Detection. *Acta Biomater.* **2013**, *9*, 6150−6157.
(4) Pouliquen, D.; Perdrisot, R.; Ermias, A.; Akoka, S.; Jallet, P.; Le Jeune, J. J. Superparamagnetic Iron Oxide Nanoparticles as a Liver MRI Contrast Agent: Contribution of Microencapsulation to Improved Biodistribution. *Magn. Reson. Imaging* **1989**, *7*, 619−27.
(5) Bulte, J. W. M.; Kraitchman, D. L. Iron Oxide MR Contrast Agents for Molecular and Cellular Imaging. *NMR Biomed.* **2004**, *17*, 484−499.
(6) Long, J. W.; Logan, M. S.; Rhodes, C. P.; Carpenter, E. E.; Stroud, R. M.; Rolison, D. R. Nanocrystalline Iron Oxide Aerogels as Mesoporous Magnetic Architectures. *J. Am. Chem. Soc.* **2004**, *126*, 16879−16889.
(7) Gupta, A. K.; Gupta, M. Synthesis and Surface Engineering of Iron Oxide Nanoparticles for Biomedical Applications. *Biomaterials* **2005**, *26*, 3995−4021.
(8) Herrera, A. P.; Barrera, C.; Rinaldi, C. Synthesis and Functionalization of Magnetite Nanoparticles with Aminopropylsilane and Carboxymethyldextran. *J. Mater. Chem.* **2008**, *18*, 3650−3654.
(9) Hong, S.; Chang, Y.; Rhee, I. Chitosan-Coated Ferrite (Fe_3O_4) Nanoparticles as a T2 Contrast Agent for Magnetic Resonance Imaging. *J. Korean Phys. Soc.* **2010**, *56*, 868−873.
(10) Shtykova, E. V.; Huang, X.; Remmes, N.; Baxter, D.; Stein, B.; Dragnea, B.; Svergun, D. I.; Bronstein, L. M. Structure and Properties of Iron Oxide Nanoparticles Encapsulated by Phospholipids with Poly(ethylene glycol) Tails. *J. Phys. Chem. C* **2007**, *111*, 18078−18086.
(11) Pellegrino, T.; Manna, L.; Kudera, S.; Liedl, T.; Koktysh, D.; Rogach, A. L.; Keller, S.; Raedler, J.; Natile, G.; Parak, W. J. Hydrophobic Nanocrystals Coated with an Amphiphilic Polymer Shell: A General Route to Water Soluble Nanocrystals. *Nano Lett.* **2004**, *4*, 703−707.
(12) Zhang, F.; Lees, E.; Amin, F.; Rivera-Gil, P.; Yang, F.; Mulvaney, P.; Parak, W. J. Polymer-Coated Nanoparticles: A Universal Tool for Biolabelling Experiments. *Small* **2011**, *7*, 3113−3127.
(13) Shtykova, E. V.; Huang, X.; Gao, X.; Dyke, J. C.; Schmucker, A. L.; Dragnea, B.; Remmes, N.; Baxter, D. V.; Stein, B.; Konarev, P. V.; Svergun, D. I.; Bronstein, L. M. Hydrophilic Monodisperse Magnetic Nanoparticles Protected by an Amphiphilic Alternating Copolymer. *J. Phys. Chem. C* **2008**, *112*, 16809−16817.
(14) Das, M.; Mishra, D.; Maiti, T. K.; Basak, A.; Pramanik, P. Bio-Functionalization of Magnetite Nanoparticles Using an Amino-phosphonic Acid Coupling Agent: New, Ultradispersed, Iron-Oxide Folate Nanoconjugates for Cancer-Specific Targeting. *Nanotechnology* **2008**, *19*, 415101/1−415101/14.
(15) Liu, G.; Swierczewska, M.; Lee, S.; Chen, X. Functional Nanoparticles for Molecular Imaging Guided Gene Delivery. *Nano Today* **2010**, *5*, 524−539.
(16) Lee, J.-H.; Schneider, B.; Jordan, E. K.; Liu, W.; Frank, J. A. Synthesis of Complexable Fluorescent Superparamagnetic Iron Oxide Nanoparticles (FL SPIONs) and Cell Labeling for Clinical Application. *Adv. Mater. (Weinheim, Ger.)* **2008**, *20*, 2512−2516.
(17) Larsen, E. K. U.; Nielsen, T.; Wittenborn, T.; Rydtoft, L. M.; Lokanathan, A. R.; Hansen, L.; Ostergaard, L.; Kingshott, P.; Howard, K. A.; Besenbacher, F.; Nielsen, N. C.; Kjems, J. Accumulation of Magnetic Iron Oxide Nanoparticles Coated With Variably Sized Polyethylene Glycol in Murine Tumors. *Nanoscale* **2012**, *4*, 2352−2361.
(18) Sun, J.; DuFort, C.; Daniel, M.-C.; Murali, A.; Chen, C.; Gopinath, K.; Stein, B.; De, M.; Rotello, V. M.; Holzenburg, A.; Kao, C. C.; Dragnea, B. Core-Controlled Polymorphism in Virus-Like Particles. *Proc. Natl. Acad. Sci. U. S. A.* **2007**, *104*, 1354−1359.
(19) Goicochea, N. L.; Datta, S. A. K.; Ayaluru, M.; Kao, C.; Rein, A.; Dragnea, B. Structure and Stoichiometry of Template-Directed Recombinant HIV-1 Gag Particles. *J. Mol. Biol.* **2011**, *410*, 667−680.
(20) Fields, B. N.; Knipe, D. M.; Howley, P. M. *Fields' Virology*; Wolters Kluwer Health/Lippincott Williams & Wilkins: Philadelphia, PA, USA, 2007.
(21) Porta, C.; Spall, V. E.; Loveland, J.; Johnson, J. E.; Barker, P. J.; Lomonossoff, G. P. Development of Cowpea Mosaic Virus as a High-Yielding System for the Presentation of Foreign Peptides. *Virology* **1994**, *202*, 949−955.
(22) Pokorski, J. K.; Steinmetz, N. F. The Art of Engineering Viral Nanoparticles. *Mol. Pharmaceutics* **2010**, *8*, 29−43.
(23) Allen, M.; Bulte, J. W. M.; Liepold, L.; Basu, G.; Zywicke, H. A.; Frank, J. A.; Young, M.; Douglas, T. Paramagnetic Viral Nanoparticles as Potential High-Relaxivity Magnetic Resonance Contrast Agents. *Magn. Reson. Med.* **2005**, *54*, 807−812.
(24) Yildiz, I.; Shukla, S.; Steinmetz, N. F. Applications of Viral Nanoparticles in Medicine. *Curr. Opin. Biotechnol.* **2011**, *22*, 901−908.
(25) Ren, Y.; Wong, S. M.; Lim, L. Y. Application of Plant Viruses as Nano Drug Delivery Systems. *Pharm. Res.* **2010**, *27*, 2509−2513.
(26) Huang, X.; Bronstein, L. M.; Retrum, J.; Dufort, C.; Tsvetkova, I.; Aniagyei, S.; Stein, B.; Stucky, G.; McKenna, B.; Remmes, N.; Baxter, D.; Kao, C. C.; Dragnea, B. Self-Assembled Virus-Like Particles with Magnetic Cores. *Nano Lett.* **2007**, *7*, 2407−2416.
(27) Daniel, M.-C.; Tsvetkova, I. B.; Quinkert, Z. T.; Murali, A.; De, M.; Rotello, V. M.; Kao, C. C.; Dragnea, B. Role of Surface Charge Density in Nanoparticle-Templated Assembly of Bromovirus Protein Cages. *ACS Nano* **2010**, *4*, 3853−3860.
(28) Huang, X.; Stein, B. D.; Cheng, H.; Malyutin, A.; Tsvetkova, I. B.; Baxter, D. V.; Remmes, N. B.; Verchot, J.; Kao, C.; Bronstein, L. M.; Dragnea, B. Magnetic Virus-like Nanoparticles in N. benthamiana Plants: A New Paradigm for Environmental and Agronomic Biotechnological Research. *ACS Nano* **2011**, *5*, 4037−4045.
(29) Bronstein, L. M.; Shtykova, E. V.; Malyutin, A.; Dyke, J. C.; Gunn, E.; Gao, X.; Stein, B.; Konarev, P. V.; Dragnea, B.; Svergun, D. I. Hydrophilization of Magnetic Nanoparticles with Modified Alternating Copolymers. Part 1: The Influence of the Grafting. *J. Phys. Chem. C* **2010**, *114*, 21900−21907.
(30) Shtykova, E. V.; Malyutin, A.; Dyke, J.; Stein, B.; Konarev, P. V.; Dragnea, B.; Svergun, D. I.; Bronstein, L. M. Hydrophilization of Magnetic Nanoparticles with Modified Alternating Copolymers. Part 2: Behavior in Solution. *J. Phys. Chem. C* **2010**, *114*, 21908−21913.
(31) Holder, P. G. F.; Daniel, T.; Stephanopoulos; Nicholas; Walton; Ross; Clark; Douglas, S.; Francis; Matthew, B. Dramatic Thermal Stability of Virus-Polymer Conjugates in Hydrophobic Solvents. *Langmuir* **2010**, *26*, 17383−17388.
(32) Bronstein, L. M.; Huang, X.; Retrum, J.; Schmucker, A.; Pink, M.; Stein, B. D.; Dragnea, B. Influence of Iron Oleate Complex Structure on Iron Oxide Nanoparticle Formation. *Chem. Mater.* **2007**, *19*, 3624−3632.
(33) Turpen, T. H.; Turpen, A. M.; Weinzettl, N.; Kumagai, M. H.; Dawson, W. O. Transfection of Whole Plants from Wounds Inoculated with Agrobacterium Tumefaciens Containing cDNA of Tobacco Mosaic Virus. *J. Virol. Methods* **1993**, *42*, 227−239.
(34) Porterfield, J. Z.; Dhason, M. S.; Loeb, D. D.; Nassal, M.; Stray, S. J.; Zlotnick, A. Full-Length Hepatitis B Virus Core Protein Packages Viral and Heterologous RNA with Similarly High Levels of Cooperativity. *J. Virol.* **2010**, *84*, 7174−7184.
(35) Ludtke, S. J.; Baldwin, P. R.; Chiu, W. EMAN: Semiautomated Software for High-Resolution Single-Particle Reconstructions. *J. Struct. Biol.* **1999**, *128*, 82−97.
(36) Blanchet, C. E.; Zozulya, A. V.; Kikhney, A. G.; Franke, D.; Konarev, P. V.; Shang, W.; Klaering, R.; Robrahn, B.; Hermes, C.; Cipriani, F.; Svergun, D. I.; Roessle, M. Instrumental Setup for High-Throughput Small- and Wide-Angle Solution Scattering at the X33 Beamline of EMBL Hamburg. *J. Appl. Crystallogr.* **2012**, *45*, 489−495.
(37) Konarev, P. V.; Volkov, V. V.; Sokolova, A. V.; Koch, M. H. J.; Svergun, D. I. PRIMUS: a Windows PC-Based System for Small-Angle Scattering Data Analysis. *J. Appl. Crystallogr.* **2003**, *36*, 1277−1282.
(38) Svergun, D. I. Determination of the regularization parameter in indirect-transform methods using perceptual criteria. *J. Appl. Crystallogr.* **1992**, *25*, 495−503.

DOI: 10.1021/acsami.5b02278
ACS Appl. Mater. Interfaces 2015, 7, 12089−12098

(39) Na, H. B.; Song, I. C.; Hyeon, T. Inorganic Nanoparticles for MRI Contrast Agents. *Adv. Mater. (Weinheim, Ger.)* **2009**, *21*, 2133−2148.
(40) Laurent, S.; Forge, D.; Port, M.; Roch, A.; Robic, C.; Vander Elst, L.; Muller, R. N. Magnetic Iron Oxide Nanoparticles: Synthesis, Stabilization, Vectorization, Physicochemical Characterizations, and Biological Applications. *Chem. Rev. (Washington, DC, U. S.)* **2008**, *108*, 2064−2110.
(41) McLachlan, S. J.; Morris, M. R.; Lucas, M. A.; Fisco, R. A.; Eakins, M. N.; Fowler, D. R.; Scheetz, R. B.; Olukotun, A. Y. Phase I Clinical Evaluation of a New Iron Oxide MR Contrast Agent. *J. Magn. Reson. Imaging* **1994**, *4*, 301−7.
(42) Li, W.; Tutton, S.; Vu, A. T.; Pierchala, L.; Li, B. S.; Lewis, J. M.; Prasad, P. V.; Edelman, R. R. First-Pass Contrast-Enhanced Magnetic Resonance Angiography in Humans Using Ferumoxytol, a Novel Ultrasmall Superparamagnetic Iron Oxide (USPIO)-Based Blood Pool Agent. *J. Magn. Reson. Imaging* **2005**, *21*, 46−52.
(43) Kircher, M. F.; Weissleder, R.; Josephson, L. A Dual Fluorochrome Probe for Imaging Proteases. *Bioconjugate Chem.* **2004**, *15*, 242−248.
(44) Carril, M.; Fernandez, I.; Rodriguez, J.; Garcia, I.; Penades, S. Gold-Coated Iron Oxide Glyconanoparticles for MRI, CT, and US Multimodal Imaging. *Part. Part. Syst. Charact.* **2014**, *31*, 81−87.
(45) Ahmad, T.; Iqbal, Y.; Bae, H.; Rhee, I.; Hong, S.; Chang, Y.; Lee, J. Relaxivities of Hydrogen Protons in Aqueous Solutions of Gold-Coated Manganese Ferrite Nanoparticles. *J. Korean Phys. Soc.* **2013**, *62*, 1696−1701.
(46) Lucas, R. W.; Larson, S. B.; McPherson, A. The Crystallographic Structure of Brome Mosaic Virus. *J. Mol. Biol.* **2002**, *317*, 95−108.
(47) Wynne, S. A.; Crowther, R. A.; Leslie, A. G. W. The Crystal Structure of the Human Hepatitis B Virus Capsid. *Mol. Cell* **1999**, *3*, 771−780.
(48) Steinmetz, N. F.; Manchester, M. PEGylated Viral Nanoparticles for Biomedicine: The Impact of PEG Chain Length on VNP Cell Interactions in Vitro and ex Vivo. *Biomacromolecules* **2009**, *10*, 784−792.
(49) Kim, P.-H.; Sohn, J.-H.; Choi, J.-W.; Jung, Y.; Kim, S. W.; Haam, S.; Yun, C.-O. Active Targeting and Safety Profile of PEG-Modified Adenovirus Conjugated with Herceptin. *Biomaterials* **2011**, *32*, 2314−2326.

DOI: 10.1021/acsami.5b02278
ACS Appl. Mater. Interfaces 2015, 7, 12089−12098